

Fibre-optic Probe Design with Side-Surface Interface

Makoto Tsubokawa

Waseda University, 2-7 Hibikino, Wakamatsu, Kitakyusyu, Japan

Keywords: Fibre-optic Sensor, Optical Probe, Optical Fibre, Optical Waveguide, Light Concentrator.

Abstract: We proposed a fibre-optic needle probe with a side-surface interface, and evaluated the normalized received power as the ratio of the signal power to source power by using ray-trace simulation. Our probe with a 1-mm diameter and 50-mm length demonstrated its performance in the sensing of target objects over a surrounding space of ~20-mm radius with a normalized received power of 0.01–10%. We also described the optimized design of the probe for use in water, and a technique used to sense targets distributed along a fibre axis with simple rotation of the probe.

1 INTRODUCTION

Because of their thin structure and ease of fabrication, there have been many studies on light concentrators with acceptance top/side surfaces of planar waveguides/optical fibres. Most of them are relevant to the well-known luminescent solar concentrator (van Sark, 2008; McIntosh, 2007; Edelenborsch, 2013); in contrast, simple concentrator that directly collect illumination light have not been fully explored because of their low efficiency (Kim, 2012). However, this simple scheme appears to be attractive for optical sensor applications because it may produce versatile applications by expanding the optical interface from a point to the surface. As an interesting example, the integration of optical fibres into textile structures called photonic textiles has been proposed to realize multifunctional sensors such as wearable photodetectors (PDs) or direction sensors of light beams (Cho, 2010; Rothmaier, 2008; Abouraddy, 2007). We are currently studying this technique to enable their application as thin optical probes used to sense the surroundings. In general, such optical probes need to incorporate micro-lens systems or several optical fibres, and should sweep over the target space because a point detector only gets a point image (Lorenser, 2011; Sampson, 2011; Wang, 2008; Piao, D., 2006; Dam, 2001; Ansari, 1993). If the detection through the side-surface interface is applicable, it may not only simplify the sweep mechanism but also enable us to realize passive optical probes without the need for precise lens

systems.

In this study, we show a new design of thin fibre-optic probe with a side surface interface, and evaluate basic characteristics by performing ray-trace simulations (LightTools, Synopsys, Inc.). Both light source (LS) for illuminating target objects and a PD are attached to the end of an optical fibre, and the light propagation through a side surface is adjusted by a Mie scattering layer embedded in the optical fibre. We show the output signal of the probe as a function of the size, position and materials comprising the target object, and finally evaluate the spatial distribution of the target and its resolution.

2 FIBRE-OPTIC PROBE MODEL

Figure 1 shows the probe model consisting of two serially concatenated guides and sensor parts. The parameters used in our simulation for the waveguide and light source are listed in Table 1. The guide part has a two-layered structure with an outer coating as an absorber in which the core guiding input light from a light source is embedded in the bottom of the cladding in addition to a normal core. A light source and PD are attached to the end face of each core. The sensor part has the scattering part at the bottom in the cladding, which is connected to the bottom core in the guide part. Light scattering is observed in the scattering part (width D) composed of a cluster of air particles with a volume density ρ . The width D is defined as the arc length corresponding to the width of the focus zone for normal incident light and

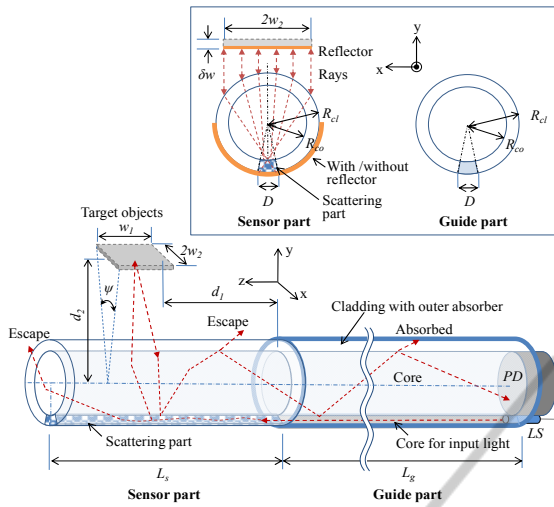
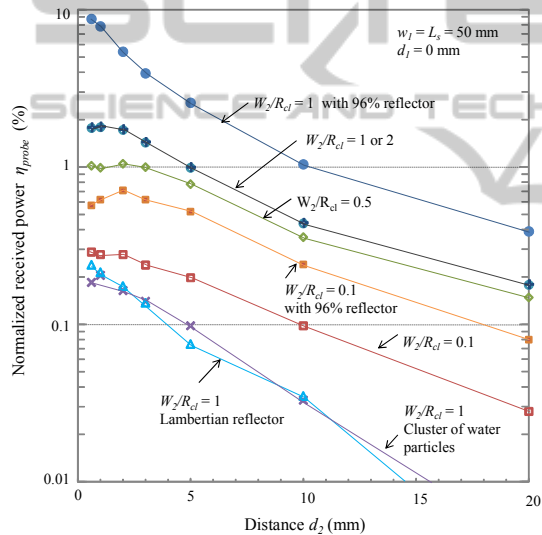


Figure 1: Fibre-optic probe model.


 Figure 2: Normalized received power η_{probe} as a function of distance d_2 and width w_2/R_{cl} .

is calculated using the size and refractive indices of the optical fibre. The minimal arrangement of the scattering part effectively generates light components in the direction of the target and suppresses excess loss during propagation along the fibre. Because of reducing D , the high index fibre is used in the simulation. Input lights are scattered in the sensor part and a portion of them reaches the target object owing to the lens effect in cylindrical optical fibre. Lights reflected at the target partially re-enter the optical fibre, and are either scattered again and transmitted to the PD or are escaped to the outside. As shown in Fig. 1, we assume the square target object of $w_1 \times 2w_2 \times \delta w$ at distances d_1 and d_2 above the sensor part. Angles ψ is the angular

Table 1: Parameters of fibre-optic probe.

| Optical fibre | Sensor part | Guide part |
|--|---|------------|
| Core radius R_{co} | 0.5 mm | |
| Cladding radius R_{cl} | 0.55mm | |
| Refractive index (core) | 1.83 | 1.83 |
| (core for input light) | 1.86 | 1.86 |
| (cladding) | 1.83 | 1.46 |
| Particle radius r | 250 nm (air) | |
| Particle density ρ | 2% | |
| Width of scattering part/ core of input light D | 0.07 mm, 0.3 mm (central angle $7.5^\circ, 31^\circ$) | |
| Length L_s, L_g | 50 mm | |

Light source (LS)

| | |
|-------------------|--|
| Input light power | 1 W |
| Wavelength | 550 nm |
| Polarization | Random |
| Position | Embedded in the end of core for input light |

Refractive indices of 1.86 (LaSFN9), 1.83 (LaSFN40), 1.46(SiO₂) are assumed. (Schott Glass Inc.)

diameter of the target. For simplicity, we assume the bottom surface of the target plane is a 96% reflector as a reference. Here we define the normalized received power η_{probe} as the ratio of light power that reaches the PD's surface by way of the target plane to the light power of the source. In our model, η_{probe} estimated by the ray-trace simulation gives results that are equivalent to the case using incoherent light without interference effects. Under the Mie scattering model used in this simulation, the wavelength dependence is almost negligible over a broadband spectrum such as natural light; therefore, we use a monochromatic source of 550-nm wavelength with a random polarisation instead of a broadband light source.

3 SIMULATION RESULTS

3.1 Normalized Received Power η_{probe}

Figure 2 shows η_{probe} , which is dependent on the distance d_2 and width w_2 . Here $d_1 = 0$ and $w_1 = L_s = 50$ mm. The particle density ρ is assumed to be 2% because η_{probe} has a maximum for this model in our simulation. Larger ρ causes not only larger scattering efficiency but also excess loss in light propagation along a fibre. Under this condition, 22% and 36% of the source power arrive at the target plane through the sensor part with and without the 96% reflector, respectively. Although these are due to scattering and lens effect in a fibre, it is fairly high efficiency without imaging optics. We can see in Fig. 2 that

η_{probe} does not vary much for $d_2 \leq 2$ mm, but above 2 mm, it tends to decrease. If the incident angle distribution to the target object is uniform, the number of round-trip rays between the sensor part and the target is roughly proportional to a half of the angular diameter $\psi(d_2)/2$, and then $\eta_{probe} \propto \psi(d_2)/2 = 2 \tan^{-1}[w_2/2d_2]$. In fact, the downward curves in Fig. 2 indicate the presence of a slightly small slope compared to the variation of $\psi(d_2)/2$ because light components with nearly normal incidence dominate owing to the lens effect in optical fibre. On the other hand, η_{probe} decreases at a rate smaller than w_2/R_{cl} because light components other than normal incidence can re-enter the sensor part when $w_2/R_{cl} < 1$. Regarding the received power, for example, η_{probe} is approximately 0.3% and 1.8% for $w_2/R_{cl} = 0.1$ and 1, respectively, at $d_2 = 2$ mm, when the sensor part has no reflector. These values are much smaller than the rate of light power that reaches the target plane as mentioned above, which suggests that the optical loss after reflection at the target plane is significant in our model. Actually, 3–4 dB loss is observed only at the boundary between the sensor and guide parts, which remains an issue. When the 96% reflector is attached to the sensor part, η_{probe} was more than doubled, i.e. 0.7% and 5% for $w_2/R_{cl} = 0.1$ and 1, respectively, at $d_2 = 2$ mm. In Fig. 2, we also plot curves for different type of targets—the Lambertian reflector and cluster of water particles as a Mie scattering object ($\delta w = 0.5$ mm, $r = 250$ -nm). They indicate that η_{probe} is smaller and more steeply decrease as compared to the case of a simple target with a reflector. These are seen as the results from the spread of the reflection angle and lower reflectivity at the target object. Next, the dependence of η_{probe} on the target length w_1 and position d_1 along a fibre axis is shown in Fig. 3. We can see that η_{probe} is nearly proportional to w_1 and it exponentially decreases with an increase in d_1 . This is because the spread of the incidence angle in the y - z plane has a similar influence on targets of different w_1 , and an increase in d_1 remarkably reduces the transmission loss along the sensor part. From these results, we can estimate the location when the target size is given, and vice versa. In fact, if we need to simultaneously sense both size and location without a sweep operation, an additional scheme is required. We discuss this issue in the next section.

3.2 Evaluation under Water Environment

Next, we consider a case involving the use of our model in water, e.g. probe biological cells in the

body. Because the refraction angle becomes small under water conditions, we designed another probe structure with width D calculated to be 0.3 mm according to the definition. Figures 4(a) and (b) show the η_{probe} as a function of distance d_2 under the water condition. Here target objects of 1.1×50 mm are (a) 96% reflector and (b) examples of Mie models and biological objects with $\delta w = 1$ mm.

We see in Fig. 4(a) that η_{probe} is obviously improved at $D = 0.3$ mm compared to $D = 0.07$ mm in the short d_2 region for the case with/without reflector on the sensor part. For a distance of $d_2 > 5$ mm, the advantage decreases when using the sensor part without the reflector. This is because the number of scattered rays for the target is increased at an optimum $D (= 0.3$ mm), but the number of round-trip rays decrease as d_2 increases owing to the

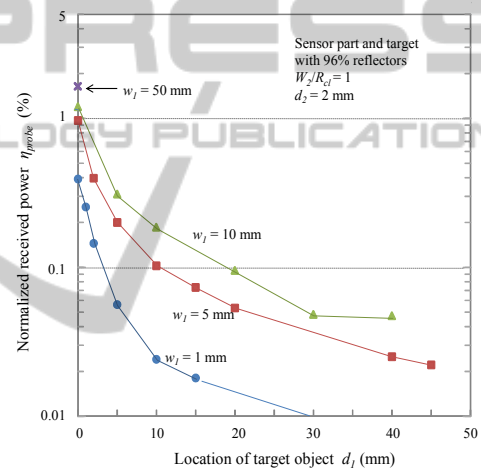


Figure 3: Normalized received power η_{probe} as a function of location d_1 and length w_1 .

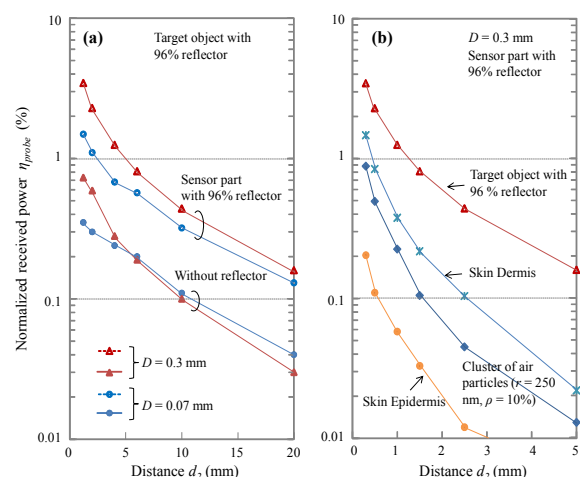


Figure 4: Normalized received power η_{probe} as a function of d_2 under water conditions. The thickness δw of skin dermis, epidermis and cluster of air particles are 1 mm.

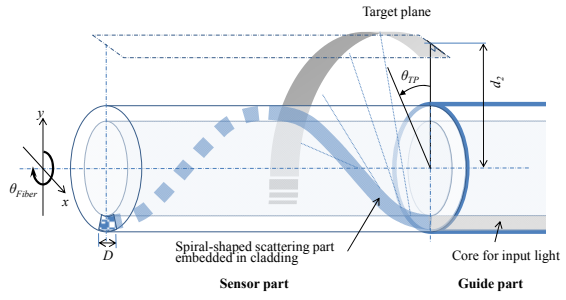


Figure 5: Fibre-optic probe with spiral-shaped scattering part.

degradation of the directional property with the increase in D . The effect of the directional property is mitigated by putting a reflector on the sensor part. In Fig. 4(b), we see that the skin dermis shows a higher reflectivity compared to the epidermis and Mie model of air particles (LightTools, Synopsys, Inc.). These results mainly indicate the differences of the reflectivity of the objects, which are useful when discerning target objects.

3.3 Evaluation of Spatially Distributed Targets

When an optical needle probe with a point detector is applied to sense a 3D space, it usually needs to be swept over the target plane; moreover, the time/frequency domain immersion or OCT techniques are usually applied to resolve the depth information. Here we focus on the approach that is used to simplify the sweep operation and set aside the techniques of immersion or OCT. Because our method can extract the information of an object arranged linearly along the probe, the linear distribution of an object may be detected without a complex sweep operation. Figure 5 shows the sensor part, which has a spiral-shaped scattering part embedded in cladding. This is the same structure as the 360° twisted sensor part in Fig. 1. Because the sensor part has a sharp directional property for the target plane in the opposite direction (180°) against the scattering part, it can highly sense the target plane that is continuously twisted with angle θ_{TP} in Fig. 5. Here $\theta_{TP} = 360d_1/L_s^\circ$. From a different viewpoint, we can detect the distribution of the target plane positioned above the sensor part (parallelogram of dash-dotted line) when the optical fibre is rotated by $0^\circ \leq \theta_{Fibre} < 360^\circ$, where $\theta_{Fibre} = -\theta_{TP}$. Figure 6 shows the normalized received power η_{probe} as a function of θ_{Fibre} . The parameters are listed in Table 1. The reflector is similarly twisted with the scattering part on the sensor part. The curve with

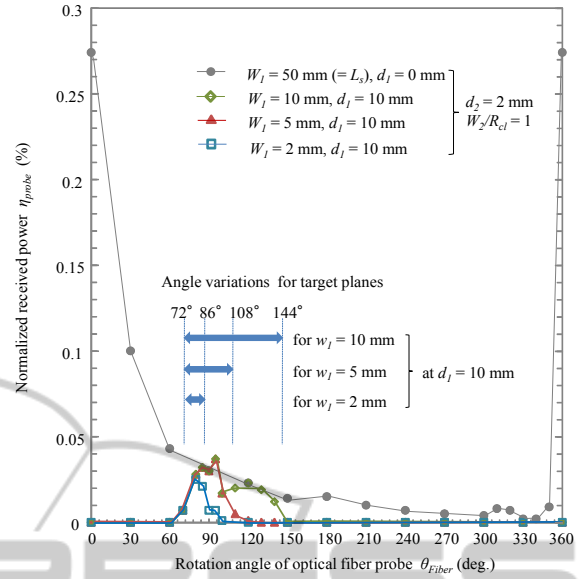


Figure 6: Normalized received power η_{probe} as a function of rotation angle θ_{Fibre} .

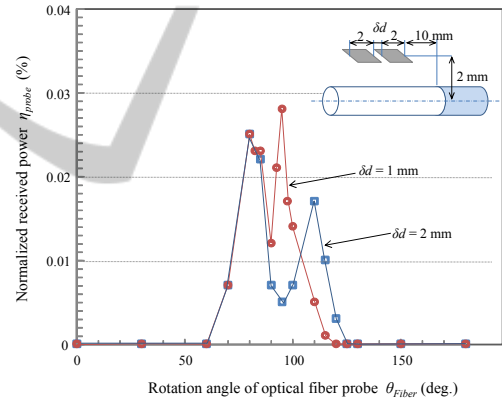


Figure 7: Curves of normalized received power η_{probe} for the targets with a small gap. Two target planes where $w_1 = 2$ mm, $w_2/R_{cl} = 1$, $d_1 = 10$ mm and $d_2 = 2$ mm are arranged in tandem with a gap δd of 1 and 2 mm.

filled circles indicates η_{probe} for the target of $w_1 = 50$ mm, $w_2/R_{cl} = 1$, $d_1 = 0$ mm and $d_2 = 2$ mm, which corresponds to the maximum η_{probe} at θ_{Fibre} and shows a steep decline with an increase in θ_{Fibre} . This tendency is similar to the results for $1 < w_1 < 5$ mm in Fig. 3. Three curves obtained for targets of $w_1 = 2, 5$ or 10 mm at $d_1 = 10$ m are also shown in Fig. 6, and the angles of peak locations and half widths of three peaks are roughly estimated to be $80, 90$ and 110° and $15, 28$ and 60° , respectively. On the other hand, four angles for locations of target edges are calculated to be $72, 86, 108$ and 144° , as shown in Fig. 6, and thus we can see that the peak locations

are in good agreement with each other, and that the half width also agrees well with the target length w_l in the region of $w_l \leq 5$ mm. As the three curves are modulated by the maximum curve (filled symbols), its peak and width tend to be fuzzy for large w_l , but they are somewhat precise for $w_l \leq 5$ mm.

Next, we evaluate two targets arranged in tandem with a small gap δd to check the spatial resolution. Figure 7 shows η_{probe} for two targets with $\delta d = 2$ mm and 1 mm, respectively. Here, $w_l = 2$ mm and $w_l/R_{cl} = 1$. Two peaks in the curve for $\delta d = 2$ mm are clearly observed, and the peak interval is estimated to be 4.2 mm for an angle difference of 30° . Because the peak location indicates the centre of the target, the peak interval is approximately given by $\delta d + w_l$ and δd is almost the same as real gap of 2 mm. For the case of $\delta d = 1$ mm, we also find two peaks with an interval of 15° , corresponding to 2.1 mm, which is slightly smaller than the expected value of 3 mm ($= \delta d + w_l$), and is caused by the peak shift effect due to the overlapping of different height pulses. Consequently, the spatial resolution is estimated to be a little less than 2 mm in this condition.

4 CONCLUSIONS

We proposed a simple fibre-optic probe with a side-surface interface against a target space, and evaluated the basic performance by performing ray-trace simulations. Our model has a needle shape of approximately 1-mm diameter and 50-mm length, which enables us to detect the normalized light power of 0.01–10% of the source power when target objects are located in a surrounding cylinder space with an ~ 20 -mm radius. Under water conditions, the sensitivity was easily improved by adjusting the size of the scattering part. Moreover, by using the directional property in the probe twisted by 360° , targets distributed along the fibre axis were also detected with less than 2-mm resolution.

In our future work, we firstly aim to improve the signal level by optimizing the probe structure and materials, for example, the shape of the fibre and particle density distribution of the scattering parts may bring about desirable effects such as narrow focus area and smooth sensitivity along a fibre. As next step aim, we need to incorporate a key technique such as the OCT technique for our method to resolve radially distributed targets.

ACKNOWLEDGEMENTS

Part of the research presented in this paper has been done under JSPS KAKENHI Grant Number 25420346.

REFERENCES

- Abouraddy, A. F., 2007. 'Towards multifunctional fibres that see, hear, sense and communicate,' *Nature Materials*, vol. 6, pp. 336–347.
- Ansari, R. R., 1993. 'Microemulsion characterization by the use of a nonvasive backscatter fibre optic probe,' *Appl. Opt.*, vol. 32, pp. 3822–3827.
- Cho, G., 2010. 'Smart clothing technology and applications,' CRC Press, Chap.5.
- Dam, J. S., 2001. 'Fibre-optic probe for noninvasive real-time determination of tissue optical properties at multiple wavelengths,' *Appl. Opt.*, vol. 40, pp. 1155–1164.
- Edelenbosch, O., 2013. 'Luminescent solar concentrators with fibre geometry,' *OSA Opt. Express*, vol. 21, pp. 503–513.
- Kim, J. M., 2012. 'Optical efficiency-concentration ratio trade-off for a flat panel photovoltaic system with diffuser type concentrator,' *Solar Energy Materials & Solar Cells*, vol. 103, pp. 35–40.
- LightTools, Synopsys, Inc., <http://www.opticalres.com/>
- Lorensen, D., 2011. 'Ultrathin side-viewing needle probe for optical coherence tomography,' *Opt. Lett.*, vol. 36, pp. 3894–3896.
- Mcintosh, K. R., 2007. 'Theoretical comparison of cylindrical and square-planar luminescent solar concentrators,' *Appl. Phys. B*, vol. 88, pp. 285–290.
- Piao, D., 2006. 'Endoscopic, rapid near-infrared optical tomography,' *Opt. Lett.*, vol. 31, pp. 2876–2878.
- Rothmaier, M., 2008. 'Photonic textiles for pulse oximetry,' *Opt. Express*, vol. 16, pp. 12973–12986.
- Sampson, D. D., 2011. 'Microscope-in-a-needle technology for deep-tissue 3D imaging,' *International Conference on Information Photonics (IP)*, pp. 1–2.
- Schott Glass Inc., <http://www.schott.com/>
- Van Sark, W. G. J. H. M., 2008. 'Luminescent solar concentrators—a review of recent results,' *Opt. Express*, vol. 16, pp. 21773–21792.
- Wang, Q., 2008. 'Measurement of internal tissue optical properties at ultraviolet and visible wavelengths: Development and implementation of a fibreoptic-based system,' *Opt. Express*, vol. 16, pp. 8685–8703.